Performance Optimization of an Electromembrane Reactor for Recycling and Resource Recovery of Desulfurization Residuals

Chenglei Yang, Ying Hu, Limei Cao, and Ji Yang
School of Resources and Environmental Engineering, State Environmental Protection Key Laboratory of Environmental Risk Assessment and Control on Chemical Process, East China University of Science and Technology, Shanghai 200237, P.R. China

DOI 10.1002/aic.14466
Published online April 23, 2014 in Wiley Online Library (wileyonlinelibrary.com)

An environmentally friendly method for electrochemically regenerating alkali-sorbent (NaOH) and recovering sulfur in the flue gas as H_2SO_4, while producing H_2 as a clean energy source from flue gas desulfurization (FGD) residuals in an electromembrane reactor, was proposed in this article. To optimize and improve the performance, the optimal operating conditions were deduced from the numerical simulation and validated using experimental data. Under the optimized conditions, the current efficiencies of alkali-sorbent regeneration and H_2SO_4 reached 84 and 87%, respectively, which is comparable to those obtained in the chlor-alkali industry. Therefore, this method has the potential to be scaled up. If this technology is integrated into an existing FGD facility, the money-consuming chemical process could be transferred into a renewable resource and clean energy conversion process. © 2014 American Institute of Chemical Engineers *AIChE J*, 60: 2613–2624, 2014
Keywords: sulfur dioxide, flue gas desulfurization, electrochemistry, electromembrane reactor, hydrogen energy

Introduction

Conventionally, commercial-scale flue gas desulfurization (FGD) technologies can be classified as once-through and regenerable depending on whether the spent sorbent is disposed.[1] In once-through technology, the spent sorbent is mainly discarded as a waste sludge or used as a by-product if possible, whereas the spent sorbent is regenerated and SO_2 is released from FGD residuals to yield sulfuric acid or elemental sulfur in regenerable technology.[2] Both once-through and regenerable processes can be further classified as wet and dry.[3] The main restraint of once-through FGD technology is the generation of huge amounts of waste sludge. Regenerable processes are preferable to once-through processes in terms of FGD residual decomposition and sorbent regeneration, but the installation is expensive and the operation is complex.[4]

Electromembrane processes, such as electrodialysis, electro–electrodialysis, and membrane electrolysis, have been developed considerably in industry, especially in the desalination of brackish water and chlorine–alkaline electrolysis.[5–7] In the past few decades, many of these techniques used in practical applications or laboratory studies directly focus on the removal of hazardous materials in effluents or gases, the recovery and reuse of valuable constituents from wastes, closing the loops in technology and new production processes that require lower energy consumption.[8] In this study, an electromembrane reactor was developed to efficiently regenerate sodium alkaline sorbent (NaOH) from FGD residuals in semidry or dry FGD processes. Subsequently, regenerated sodium hydroxide was used and recycled as a scrubbing agent for desulfurization, and elemental sulfur was recovered in the form of sulfuric acid while producing hydrogen as a clean energy. Figure 1 provided a simple block flow diagram showing all of the inputs and outputs of the designed process. This electrochemical regeneration is a feasible method to dispose FGD residuals and also a green technique because the only reagent is electrons, with little or no secondary pollution. Furthermore, the electromembrane reactor can use the surplus electricity from a power plant or inexpensive off-peak electricity, which will decrease the operation cost.[9,10]

To improve the reactor performance and optimize the operating parameters, the electrochemical regeneration process in the electromembrane reactor must be accurately analyzed, which requires complex computations.[11] Many studies have investigated the concentration profiles, potentials and ion fluxes of membrane electrolysis and its related systems using the Nernst–Planck (NP) approach.[12–15] A few recent works were used to optimize the behaviors of electromembrane processes for recovering valuable materials from FGD residuals. In this article, the mass transfer, overall potential distribution across the stack, gas-evolving electrodes, and current efficiency were discussed in detail. The effects of different factors, such as current density, feed flow rate, and initial electrolyte concentrations, were evaluated to obtain the optimized parameters.

Experimental

Materials and reagents

All reagents were purchased from the Shanghai Chemical Reagent Co. (China) and were reagent-grade or better.

Additional Supporting Information may be found in the online version of this article.

Correspondence concerning this article should be addressed to J. Yang at yangji@ecust.edu.cn.

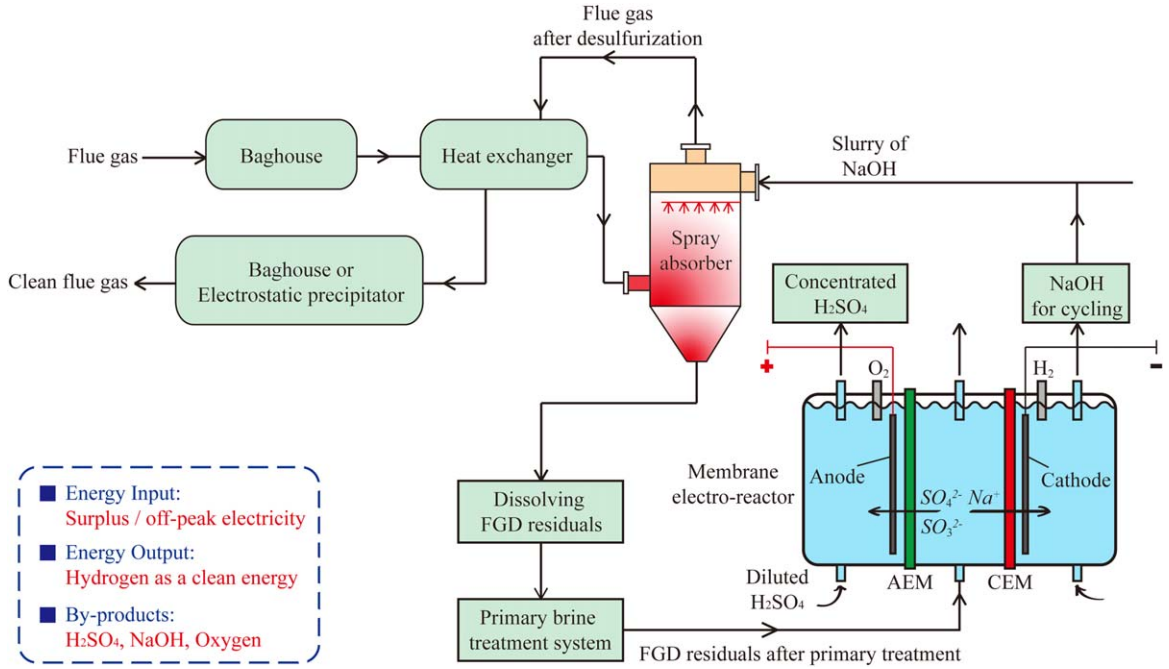

Figure 1. Schematic diagram of the designed electrochemical process for recycling and resource recovery of FGD residuals.

[Color figure can be viewed in the online issue, which is available at wileyonlinelibrary.com.]

Deionized water was used throughout the experiments to prepare the sample solutions. The practical desulfurization residuals were obtained from a semidry FGD of a Shandong Zaozhuang power plant using NaOH as the scrubbing agent. The detailed analysis of the residuals shows that it contained 82% Na_2SO_4 and 11% Na_2SO_3 by weight. The rest of the sample was composed by the oxides of Si, Fe, Al, and Ca. Before the aqueous solution of FGD residuals was introduced into the electromembrane reactor, most of calcium and magnesium including some soluble impurities were removed by chemical precipitation with NaOH in the primary brine treatment system, as shown in Table S1 in the Supporting Information. Therefore, for simplicity, the simple test solution of Na_2SO_4 was used as simulation solution of FGD residuals in the modeling and lab-scale experiments.

The volume of gaseous hydrogen was measured by the gasometrical method, wherein the gaseous hydrogen was trapped in a vessel filled with water that was itself pushed out when the hydrogen filled the tank. Therefore, the volume of hydrogen gas can be determined by simply measuring the volume of the displaced water.

Furthermore, all the experiments were conducted three times to check the reproducibility of the results, and the agreement between successive experiments was within ±5%. The entire numerical simulation and calculation can be performed with Wolfram *Mathematica*® 8 (Wolfram Research) and MS Excel (Microsoft Corporation).

Electromembrane reactor

A lab-scale electromembrane reactor was developed, as shown in Figure 2. The reactor was composed of an anode (26 × 13 cm) and a cathode (26 × 13 cm) placed 1.5 cm apart from one another and 3.0 cm from the reactor wall. Ti–IrO_2 was chosen as the anode and Ti as the cathode for the electrochemical reactor. The reactor was divided into three compartments by a cation-exchange membrane (JCM-II, Wuxi Jianyi Co., Wuxi, Jiangsu, China) and an anion-exchange membrane (JAM-II, Wuxi Jianyi Co.). The effective surface area of each membrane was 338 cm^2, and the other properties of the membranes were introduced in Table 1. In this lab-scale setup, Na_2SO_4, H_2SO_4, and NaOH solutions were introduced into the corresponding compartments and the reactor was operated in a batch mode by continuous recycling via three peristaltic pumps (Baoding Longer Precision Pump Co., China). A direct current (DC) voltage-stabilized power supply (Shanghai Liyou Electrification Co., China) was used to control the potential.

Theoretical basis

Summary. When the designed electromembrane reactor in this study was charged at a constant current density, the Na^+ and the SO_4^{2-} in the middle compartment migrated through the cation-exchange membrane and anion-exchange membrane, respectively, based on the selective permeability of the membranes. The oxygen and hydrogen evolution reactions (HERs) are the main reactions during electrochemical separation and regeneration, as shown in following equations.

$$\text{Cathode:}\quad 4Na^+ + 4H_2O + 4e \rightarrow 4NaOH + 2H_2\uparrow \qquad (1)$$

$$\text{Anode:}\quad 2SO_4^{2-} + 2H_2O \rightarrow 2H_2SO_4 + O_2\uparrow + 4e \qquad (2)$$

$$\text{Overall reaction:}\quad 2H_2O \rightarrow 2H_2\uparrow + O_2\uparrow \qquad (3)$$

The basic expression of the overall potential for a single cell is shown in Eq. 4

$$E_{cell} = E_{eq} + \eta_a + (-\eta_c) + IR_m + IR_s \qquad (4)$$

where E_{eq} is the theoretical equilibrium potential (V) of the cell; η_a (V) and η_c (V) are the overpotential on the anode

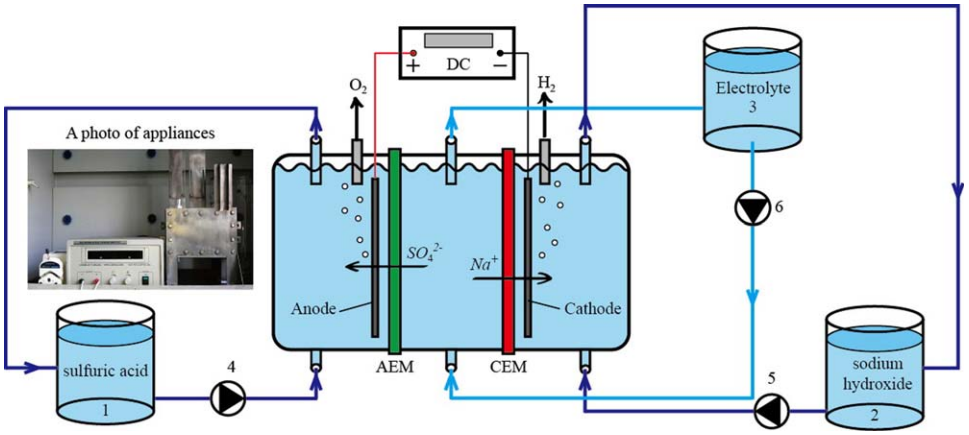

Figure 2. Schematic diagram of a lab-scale electromembrane reactor. (1, 2, 3) Reservoir of H_2SO_4, NaOH, and Na_2SO_4, respectively; (4, 5, 6) Peristaltic pump.

[Color figure can be viewed in the online issue, which is available at wileyonlinelibrary.com.]

and cathode, respectively; and IR_m and IR_s are the voltage losses associated with the conductivity of the membranes and electrolyte, respectively. The IR loss is called the ohmic overpotential.

Ideally, an electrochemical process features high current efficiency. The current efficiency of H_2SO_4 and NaOH can be calculated as follows

$$H_2SO_4: \quad \eta = \frac{2(C_t - C_0)VF}{It} \tag{5}$$

$$NaOH: \quad \eta = \frac{(C_t - C_0)VF}{It} \tag{6}$$

where C_t and C_0 (mol L^{-1}) are the concentration of the acid or base at time t and 0, respectively; V (L) is the circulated volume of solution, that is, 0.70 L in the lab-scale reactor; F is the Faraday constant (96,485 C mol^{-1}); and I (A) is the current.

Equilibrium Potential. As mentioned earlier, the overall electrochemical reaction is the electrolysis of water, shown in Eq. 3. It is assumed that the cell consisted of a titanium electrode and a Ti–IrO_2 electrode submerged in the electrolyte. The electrochemical process would occur if a voltage drop greater than its electromotive force were applied to the cell. The electromotive force can be calculated by the Nernst equation.

In an electrochemical cell, the overall electromotive force can also be defined as the potential difference between the anode (E_{an}) and cathode (E_{cat}).[16] This potential difference is related to the Gibbs energy change as shown in Eq. 7

$$\Delta G = -nFE = -nF(E_{an} - E_{cat}) \tag{7}$$

The Gibbs energy is related to the entropy by $\Delta G = \Delta H - T\Delta S$, where H is the enthalpy, S is the entropy, and T is the temperature of the system. Under standard conditions, the standard cell electromotive force can be expressed by $E_0 = -\Delta G^0/nF$. To achieve hydrogen and oxygen production by water electrolysis, an equilibrium cell voltage, also called the reversible electromotive force, must be overcome. The equilibrium potential, E_{eq} (standard conditions, 25°C, 1 bar) is equal to 1.23 V using the literature values of the standard-state entropy change for the overall reaction.[17] However, because of the activation energy barrier, the low reaction rate and bubble formation, an overpotential (η) above the equilibrium cell voltage is needed to excite the inherently slow electrode reactions, even when the equilibrium potential is met.[18]

Cathode Overpotential. The widely accepted mechanism of HER in alkaline solution consists of the following three steps involving the formation of absorbed hydrogen on the cathode surface.[19,20]

$$\text{Volmer step:} \quad H_2O + M + e^- \leftrightarrow MH_{ads} + OH^- \tag{8}$$

$$\text{Heyrovsky step:} \quad H_2O + MH_{ads} + e^- \leftrightarrow H_2 + M + OH^- \tag{9}$$

$$\text{Tafel step:} \quad MH_{ads} + MH_{ads} \leftrightarrow H_2 + 2M \tag{10}$$

where M represents the active site of the metal on the electrode surface and MH_{ads} is the hydrogen absorbed on the electrode surface. Based on these three steps, the Volmer–Tafel or Volmer–Heyrovsky (V–H) reaction sequences are the possible mechanisms.[21] Thus, for the V–H mechanisms, neglecting Tafel step, the rate equations for the corresponding V–H steps are

$$v_1 = k_1(1-\theta)a_{H_2O}\exp(-\alpha_1 fE) - k_{-1}\theta a_{OH^-}\exp[(1-\alpha_1)fE] \tag{11}$$

$$v_2 = k_2\theta a_{H_2O}\exp(-\alpha_2 fE) - k_{-2}(1-\theta)a_{OH^-}\exp[(1-\alpha_2)fE] \tag{12}$$

$$\frac{i}{F} = v_1 + v_2 \tag{13}$$

where θ is the coverage of the absorbed intermediate H_{ads}; E is the electrode potential; α_i (i = 1, 2) is the symmetry factor; k_1 and k_2 are the rate constants in the forward direction; k_{-1} and k_{-2} are the rate constants in the backward direction, and f is equal to F/RT. Previous studies have concluded that the

Table 1. The Properties of the Ion-Exchange Membranes Used in the Designed Reactor

Membrane	Thickness (mm)	Exchange capacity (meq/g)	Water content (%)	Area resistance (Ω cm^2)	Transport number (%)	Average LCD[a] (mA cm^{-2})
JCM-II	0.20	1.8–2.0	33–38	3–6	85–90	7.4
JAM-II	0.20	1.6–1.8	22–24	6–10	90–95	7.4

[a]The average limiting current density (LCD) of the membrane was determined with a certain electrolyte concentration ranging from 0.35 to 1.40 mol L^{-1} and different retention times in this study.

HER proceeded through V–H mechanisms and was controlled by a Heyrovsky step.[19,20,22] Therefore, the kinetic expression can be written as Eq. 14, assuming that the Heyrovsky step is the rate-determining step (RDS) and that the Volmer step is at quasiequilibrium

$$\frac{i}{F}=k_2\theta a_{H_2O}\exp(-\alpha_2 fE)-k_{-2}(1-\theta)a_{OH^-}\exp[(1-\alpha_2)fE] \quad (14)$$

At the equilibrium electrode potential, Eq. 14 can be rewritten as Eq. 15

$$\frac{i_o}{F}=k_2\theta_e a_{H_2O}\exp(-\alpha_2 fE_e)=k_{-2}(1-\theta_e)a_{OH^-}\exp[(1-\alpha_2)fE_e] \quad (15)$$

where i_o is the exchange current density, which is related to the nature of the electrode materials; θ_e is the equilibrium coverage of absorbed H_{ads}, and E_e is the equilibrium electrode potential. Dividing Eq. 14 by Eq. 15 yields

$$i=i_o\left\{\frac{\theta}{\theta_e}\exp(-\alpha_2 f\eta_c)-\frac{1-\theta}{1-\theta_e}\exp[(1-\alpha_2)f\eta_c]\right\} \quad (16)$$

where η_c is the overpotential at the cathode and $\eta_c=E-E_e$. This analogous derivation of the Butler–Volmer equation describes the HER kinetics. From the equation above, at a large negative overpotential, $e^{-\alpha_2 f\eta_{cat}} \gg e^{(1-\alpha_2)f\eta_{cat}}$ and the expression of η_c can be approximated as Eq. 17

$$-\eta_c=\frac{RT}{\alpha_2 F}\left(\ln\frac{i}{i_{c,\ o}}-\ln\frac{\theta}{\theta_e}\right) \quad (17)$$

Anode Overpotential. The oxygen evolution reaction (OER) mechanism, which depends on the oxide composition and the potential range, is more complex than the HER. Generally, the most accepted mechanism for the OER in acid media is as follows[23]

$$S+H_2O \rightarrow S{-}OH_{ads}+H^++e^- \quad (18)$$

$$S{-}OH_{ads} \rightarrow S{-}O_{ads}+H^++e^- \quad (19)$$

$$S{-}OH_{ads}+S{-}OH_{ads} \rightarrow S{-}O_{ads}+H_2O \quad (20)$$

$$S{-}O \rightarrow 1/2O_2+S \quad (21)$$

where S is the active site on the anode oxide surface and $S{-}OH_{ads}$ and $S{-}O_{ads}$ are two intermediates. Reactions 19 and 20 are alternatives, and the occurrence of one or the other depends on the bond strength of the intermediate. In the high-potential domain, reaction 18 may be substituted by the following two steps[23,24]

$$S+H_2O \rightarrow S{-}OH^*_{ads}+H^++e^- \quad (22)$$

$$S{-}OH^*_{ads} \rightarrow S{-}OH_{ads} \quad (23)$$

where $S{-}OH^*_{ads}$ and $S{-}OH_{ads}$ have the same chemical structure but different energy states. Both reactions 22 and 23 have been reported as the OER mechanism when the other reactions were fast.[23–25] At high potentials, reaction 22 is generally considered as the RDS.[24] Therefore, the kinetic equations of the OER can be derived as Eq. 24, in which θ^* is the coverage of the $S{-}OH^*_{ads}$ intermediate and θ^*_e is the corresponding equilibrium coverage

$$i=i_o\frac{1-\theta^*}{1-\theta_e{}^*}\exp(\beta_1 f\eta_a) \quad (24)$$

Rearranging the equation above, the anode overpotential, η_a, can be described as follows

$$\eta_a=\frac{RT}{\beta_1 F}\left(\ln\frac{i}{i_{a,o}}-\ln\frac{1-\theta^*}{1-\theta_e{}^*}\right) \quad (25)$$

where β_1 is the symmetry factor and $i_{a,o}$ is the exchange current density of the anode. By comparison with the Tafel equation in the literature,[16] a term related to surface coverage was added into the expressions of η_a and η_c.

Ohmic Overpotential. The electrical resistances lead to the waste of electrical energy in the form of heat according to Ohm's Law. In the proposed electromembrane cell, the electrical resistances mainly consisted of two parts: the resistance in the electrolyte due to the ion transfer and formation of gas bubbles and the resistance of the membranes.

First, the *IR* drop within the electrolyte solution is obtained by the following Eq. 26

$$IR_s=il/\kappa \quad (26)$$

where i is the current density (A cm^{-2}); l (cm) is the spacing of the compartment, wherein the cathode chamber is 3 cm, the anode chamber is 3 cm, and the middle chamber is 1.5 cm; κ (Ω^{-1} cm^{-1}) is the conductivity of the electrolyte. Because the flow field of the electrolyte influences the ionic transfer, temperature distribution and bubble size, the convective mass transfer and bubble effects should be considered. In particular, the bubble effects will reduce the effective area of the electrodes and decrease the conductivity of the electrolyte. Thus, an empirical equation was introduced to estimate the effects of the bubbles on the electrolyte conductivity[26]

$$\kappa=\kappa_o(1-\varepsilon)^{3/2} \quad (27)$$

where ε is the void fraction caused by bubble formation and κ_o, calculated by Eq. 28, is the conductivity of the gas-free solution[27]

$$\kappa_o=\Lambda C_b=\left[\Lambda^\circ(t)-A(t)\frac{m^{0.5}}{1+Bm^{0.5}}\right]C_b \quad (28)$$

where Λ° (cm^2 Ω^{-1} mol^{-1}), a function of temperature, is the molar conductivity at infinite dilution; C_b is the molar concentration of the electrolyte in the bulk solution; A(t) is a function of temperature; B is the empirical constant; and m is the molality of the electrolyte in the bulk solution. Therefore, the *IR* drop within the electrolyte can be estimated by the equation sequence from Eqs. 26 to 28.

The resistance to the ion flow in the membrane can be defined as Eq. 29

$$IR_m=i\delta/\kappa_m \quad (29)$$

where δ (cm) is the average thickness of the membrane and κ_m (Ω^{-1} cm^{-1}) is the membrane conductivity, which is a complicated function of water content, the nature of the membrane, ionic form, pH, and the operating parameters, such as temperature, the concentration of the electrolyte in contact with the membrane, and the current density. An empirical expression for Nafion membrane resistivity was proposed by Mann et al.[28] and is shown in Eq. 30

$$\kappa_m=\frac{1}{r_m}=\frac{(\lambda-0.634-3i)\exp\left[4.18\left(\frac{T-303}{T}\right)\right]}{181.6[1+0.03i+0.062\left(\frac{T}{303}\right)^2 i^{2.5}]} \quad (30)$$

where λ is an adjustable parameter with a maximum possible value of 23. This parameter will be influenced by the

membrane preparation procedure and may be a function of the relative humidity, stoichiometric ratio of the feed gas, and time-for-service of the membrane.[28] T is the cell temperature in kelvin. In this article, Eq. 30 was used to estimate the value of κ_m. Therefore, the *IR* drop of the membrane can be estimated by Eqs. 29 and 30.

Mass Transfer. The optimization of an electrochemical process is based on a number of parameters, such as spacer configuration, membrane properties, feed and production concentration, feed flow velocity, and current density.[29] Current is the driving force of the electromigration of charged species in the membrane electrolysis processes. Here, for simplicity, it was assumed that the electrolytic process and mass transfer in the electromembrane reactor occurred in a one-dimensional column along the x-axis. In this study, the NP equation was used to describe the ionic transport, including diffusion and electromigration. Some other assumptions included the following: (a) boundary layers adjacent to the membranes were uniform and static, (b) the bulk solution in the chamber was completely mixed such that the concentration at any position of the electrolyte in this ozone was similar, (c) the distribution of current and pressure was uniform, and (d) there were no solution leakages in the membranes.

For linear mass transport, the flux of a certain mobile ionic species can be expressed as Eq. 31

$$N_i = -D_i\left(\frac{\partial C_i}{\partial x}\right) - \frac{z_i F}{\mathrm{RT}} D_i C_i \left(\frac{\partial \varphi}{\partial x}\right) + C_i u \tag{31}$$

where N_i, D_i, C_i, and z_i represent the flux of a mobile ionic species, the diffusion coefficient, the concentration of component i, and the charge of the ionic species, respectively. F is the Faraday constant, R is the universal gas constant, T is the absolute temperature, φ is the electrical potential, and u is the flow velocity. The terms on the right-hand side represent the contributions of diffusion, migration, and convection in turn. Species i can be Na^+, SO_4^{2-}, H^+, or OH^-, which are referred to species 1, 2, 3, and 4, respectively. The flux of species i contributed by migration can be written as Eq. 32[30]

$$\frac{t_i j}{z_i F} = \frac{z_i F D_i}{\mathrm{RT}} C_i \frac{\partial \varphi}{\partial x} \tag{32}$$

where t_i is the transference number of species i, and j is the current density (to distinguish between the subscript i and current density). The ion flux through the membrane was represented as the sum of the migration and diffusion as follows[13]

$$N_m = \frac{t_m i}{F} + N_{m,d} = \frac{t_m i}{F} + \frac{D_m \Delta C}{\delta_m} \tag{33}$$

where t_m is the ion transport number in the cation- or anion-exchange membrane, D_m is the diffusion coefficient in the membrane, ΔC is the concentration difference, and δ_m is the average thickness of the membrane.

Therefore, the mass balance in the electromembrane processes can be expressed by the following equations.

Cathode chamber

$$V_{cat}\frac{dC_{1,cat}}{dt} = QC_{1,in} - QC_{1,cat} + \frac{t_{1,m} I}{F} + \frac{A_m D_{1,m}(C^s_{1,mid} - C^s_{1,cat})}{\delta_c} \tag{34}$$

Anode chamber

$$V_{an}\frac{dC_{2,an}}{dt} = QC_{2,in} - QC_{2,an} + \frac{t_{2,m} I}{2F} + \frac{A_m D_{2,m}(C^s_{2,mid} - C^s_{2,an})}{\delta_a} \tag{35}$$

Middle chamber

$$V_{mid}\frac{dC_{i,mid}}{dt} = QC_{i,in} - QC_{i,mid} - \frac{t_{i,m} I}{z_i F} - \frac{A_m D_{i,m}(C^s_{i,mid} - C^s_{i,chamber})}{\delta_m} \tag{36}$$

Reservoir of NaOH

$$V_T\frac{dC_{1,in}}{dt} = QC_{1,cat} - QC_{1,in} \tag{37}$$

Reservoir of H_2SO_4

$$V_T\frac{dC_{2,in}}{dt} = QC_{2,an} - QC_{2,in} \tag{38}$$

Reservoir of middle chamber

$$V_T\frac{dC_{i,midin}}{dt} = QC_{i,mid} - QC_{i,midin} \tag{39}$$

where $C^s_{i,mid}$ is the concentration of species i at the membrane surface in the middle chamber; $C^s_{1,cat}$ and $C^s_{2,an}$ represent the concentration of Na^+ and SO_4^{2-} at the membrane surface in the cathode chamber and anode chamber, respectively; V_{cat}, V_{an}, V_{mid}, and V_T are the volumes of cathode chamber, anode chamber, middle chamber, and reservoirs, respectively; and Q is the fluid flow rate.

The concentration gradient at the membrane interfaces is proportional to the current density as shown in Eq. 40:[31]

$$\left(\frac{\partial C}{\partial x}\right)_{x=0} = -\frac{(t_{i,m} - t_i) i}{z_i F D_i} \tag{40}$$

The concentrations at the membrane surfaces can be deduced from Eq. 40 as follows

$$C^s_{1,cat} = C_{1,cat} + \frac{i(t_{1,m} - t_1)\delta}{D_1 F} \tag{41}$$

$$C^s_{1,mid} = C_{1,mid} - \frac{i(t_{1,m} - t_1)\delta}{D_1 F} \tag{42}$$

$$C^s_{2,an} = C_{2,an} + \frac{i(t_{2,m} - t_2)\delta}{2D_2 F} \tag{43}$$

$$C^s_{2,mid} = C_{2,mid} - \frac{i(t_{2,m} - t_2)\delta}{2D_2 F} \tag{44}$$

Results and Discussion

Overall potential distribution

Table 2 shows the values of the model parameters involved in the computer prediction. The overall potential distribution was calculated by Eqs. 4, 17, and 25–30 as shown in Table 3. All calculated values for the overall potential drop were similar to the experimental data, with a maximum deviation of less than 10%. There was a comparable increase in the *IR* drop across the electrolyte and membranes, and the increases of the overpotentials of the electrodes were small. Conversely, it was evident that the *IR* drop across the electrolyte and membranes both increased with increasing current, corresponding to lower energy efficiency. Consequently, appropriate membrane selection and a

Table 2. The Values of the Model Parameters

Parameter	Value	References
V_{cat} (volume of the cathode chamber)	0.54 L	In this work
V_{an} (volume of the anode chamber)	0.54 L	In this work
V_{mid} (volume of the middle chamber)	0.54 L	In this work
V_T (volume of the reservoir)	0.16 L	In this work
δ_a, δ_c, δ_m (average thickness of the membrane)	0.2 mm	In this work
A_m (effective surface area of the membrane)	338 cm^2	In this work
$t_{i,m}$ (ion transport number in the membrane, $i = 1, 2$ and refer to Na^+ and SO_4^{2-}, respectively)	$t_{1,m} = 0.85$ $t_{2,m} = 0.95$	15
t_i (ion transport number in the corresponding aqueous solution, $i = 1, 2$ and refer to Na^+ and SO_4^{2-}, respectively)	$t_1 = 0.39$ $t_2 = 0.63$	32
$D_{1,m}$ (diffusion coefficient of Na^+ in the membrane)	10^{-10} m^2 s^{-1}	33
$D_{2,m}$ (diffusion coefficient of SO_4^{2-} in the membrane)	10^{-11} m^2 s^{-1}	33
δ (thickness of the diffusion boundary layer)	Approximately 2 mm	34
θ (hydrogen coverage)	0.1	35
θ^*(the coverage of S—OH^*_{ads})	0.01	24
A_2, β_1 (symmetry factor)	$\alpha_2 = \beta_1 = 0.5$	In this work
$i_{c,o}$ (exchange current density of the cathode)	5.25×10^{-3} A cm^{-2}	36
$i_{a,o}$ (exchange current density of the anode)	10^{-5} A cm^{-2}	37

low voltage drop over the electrolyte solution were critical for guaranteeing the high efficiency of the designed reactor.

In addition to electrode, membrane, and electrolyte, the design and optimization of an electrochemical process involve a number of parameters, such as feed flow rate, feed concentration, and current density.[37] To optimize the performance of the developed reactor, the following series of experiments were executed with controlled single variables.

Electrochemical regeneration

In the present experiments, a Na_2SO_4 solution with different initial concentrations was introduced into the middle chamber of the electromembrane reactor by a peristaltic pump at room temperature. The initial concentrations of the H_2SO_4 and NaOH in the anode chamber and cathode chamber, respectively, were both about 5% (by mass). The feed flow rate was 12.12 L h^{-1} (retention time 160 s) in all three reactor compartments. The current applied by the DC power supply was 2.5 A (approximately 74 A m^{-2}) in all batch experiments. Figure 3 shows the numerical simulation results of the outlet concentration profiles of acid and base with different Na_2SO_4 initial concentrations. The findings indicated that the outlet concentrations of acid and base both increased with time, and the numerical simulation results agreed well with the experimental data. Figure 3c, d revealed a threshold value of the outlet concentration in both the anode and cathode chamber for long run times (acid: approximately 604,800 s, equivalent to 1 week; base: 10^5 s, approximately 1 day) in the numerical simulation. This threshold exists because the concentration of Na_2SO_4 in the middle chamber along with the concentration difference on both sides of the ion-exchange membrane decreased with the passage of time for the migration and diffusion to the adjacent chambers through the membrane, which increased the osmotic pressure

Table 3. Calculated Overall Potential Distribution Across the Stack

I (A)	E_{eq} (V)	η_c (V)	η_a (V)	IR_m (V)	IR_s (V)	E_{cal} (V)	E_{ex} (V)
1.5	1.23	0.11	0.55	0.0021	0.82	2.71	3.00
2.0	1.23	0.12	0.56	0.0028	1.09	3.01	3.20
2.5	1.23	0.14	0.58	0.0034	1.37	3.31	3.40
3.0	1.23	0.15	0.59	0.0041	1.64	3.60	3.70

Parameter	Equation	References
$\kappa_{m,CEM}$ (Ω cm^{-1})	$\kappa_m = \frac{1}{r_m} = \frac{(14-0.634-3i)\exp\left[4.18\left(\frac{T-303}{T}\right)\right]}{181.6\left[1+0.03i+0.062\left(\frac{T}{303}\right)^2 i^{2.5}\right]}$	28
$\kappa_{m,AEM}$ (Ω cm^{-1})	$\kappa_m = \frac{1}{r_m} = \frac{(23-0.634-3i)\exp\left[4.18\left(\frac{T-303}{T}\right)\right]}{181.6\left[1+0.03i+0.062\left(\frac{T}{303}\right)^2 i^{2.5}\right]}$	28
κ_o (NaOH) (Ω cm^{-1}) ($t = 25°C$)	$\kappa_o = \Lambda C_b = \left[\Lambda^\circ(t) - A(t)\frac{m^{0.5}}{1+Bm^{0.5}}\right]C_b$ $\Lambda^\circ(t) = 0.006936t^2 + 3.872t + 148.3$ $A(t) = 0.01018t^2 + 0.67421t + 56.76$, $B = 0.2$	27
κ_o (H_2SO_4) (Ω cm^{-1}) ($t = 25°C$)	$\kappa_o = \Lambda C_b = \left[\Lambda^\circ(t) - A(t)\frac{m^{0.5}}{1+Bm^{0.5}}\right]C_b$ $\Lambda^\circ(t) = -0.01985t^2 + 7.421t + 283.3$ $A(t) = 0.09194t^2 + 63.37t + 1869$, $B = 11.5$	27
κ_o (Na_2SO_4) (Ω cm^{-1}) ($t = 25°C$)	$\kappa_o = \Lambda C_b = \left[\Lambda^\circ(t) - A(t)\frac{m^{0.5}}{1+Bm^{0.5}}\right]C_b$ $\Lambda^\circ(t) = 0.009501t^2 + 2.317t + 66.58$ $A(t) = 0.02388t^2 + 4.509t + 135.5$, $B = 2.2$	27

$C_{0,H2SO4}$ = 0.4 mol L^{-1}, $C_{0,NaOH}$ = 0.4 mol L^{-1}, $C_{0,Na2SO4}$ = 1.0 mol L^{-1}, feed flow rate was 24.84 L h^{-1} and $t = 25°C$. E_{cal} is the calculated overall potential, and E_{ex} is the experimental value.

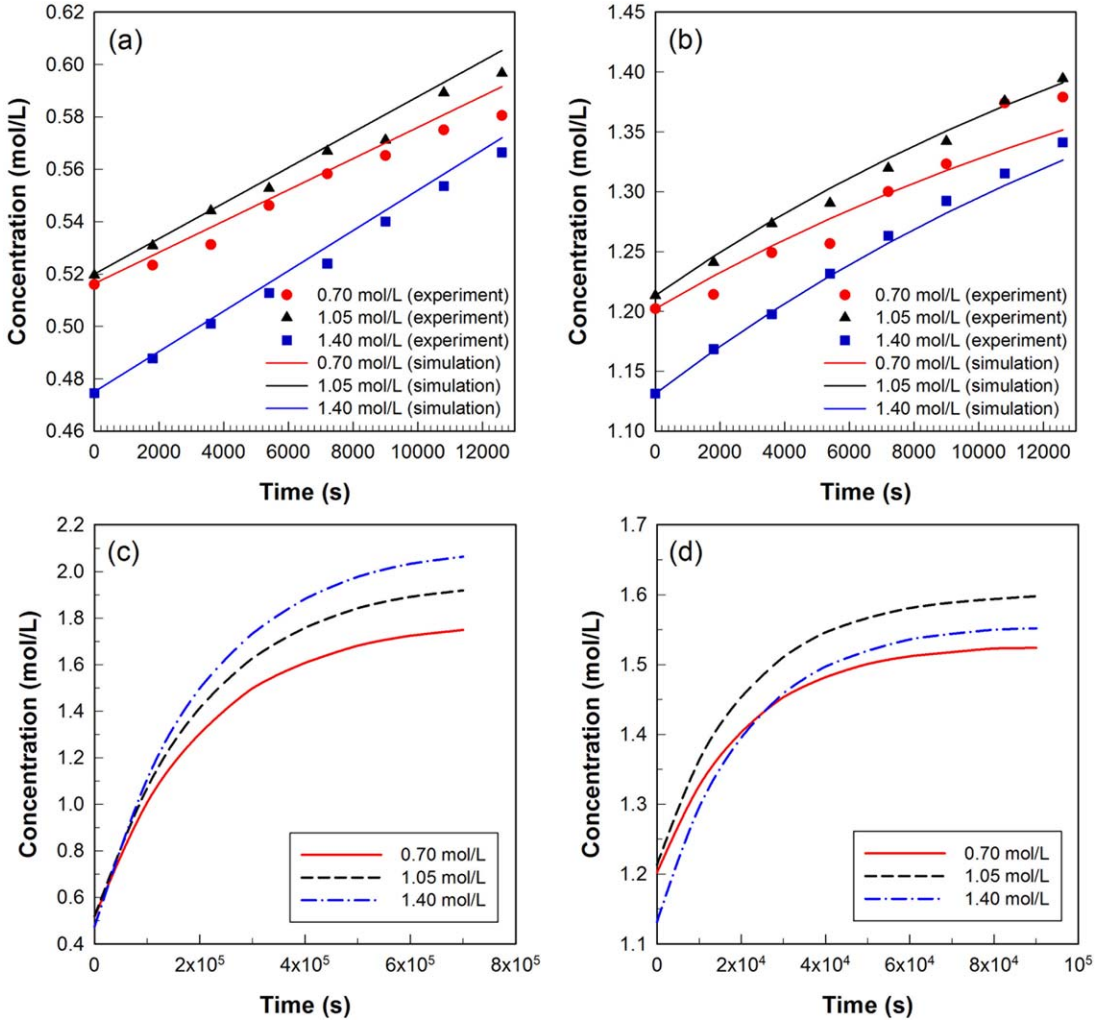

Figure 3. Acid and base outlet concentration profiles for different Na_2SO_4 initial concentrations in the middle chamber.

(a) The outlet concentration profiles of H_2SO_4 in the anode chamber compared with the experimental data and (b) The outlet concentration profiles of NaOH in the cathode chamber compared with the experimental data. (c) and (d) The outlet concentrations of acid and base, respectively, with a long running time in numerical simulations. [Color figure can be viewed in the online issue, which is available at wileyonlinelibrary.com.]

and restrained the migration of ions through the membranes. Therefore, for long running times, a threshold value could be reached. The time required to reach the threshold value was different for the acid and base most likely due to the difference in the migration and diffusion rates.

In the following experiments, the feed flow rate of all electrolyte solutions into the corresponding chambers were the same for the same batch tests but differed by batch (Figure 4). The other operating parameters were not changed. The initial concentrations of Na_2SO_4, H_2SO_4, and NaOH were approximately 1.0, 0.40, and 0.40 mol L^{-1}, respectively. The current applied was also 2.5 A. In addition, the current is the driving force of the electromigration of charged species in the membrane electrolysis process. So, in another experiment, the numerical simulation results with different current densities were compared with the experimental data, as shown in Figure 5. The other operating parameters were also unchanged. The initial concentrations of Na_2SO_4, H_2SO_4, and NaOH were approximately 1.0, 0.40, and 0.40 mol L^{-1}, respectively. The feed flow rate was 24.84 L h^{-1}. Both Figures 4 and 5 readily showed that the simulation results agreed well with the experimental data. Therefore, all results of the computer predictions with different controlled single variables presented above agreed well with the experimental data, validating the capability of the developed model for mass transfer.

Current efficiency and optimization

A mathematical expression of the acid or base outlet concentration can be obtained using Wolfram *Mathematica*® 8 to solve the differential equations in the mass transport model (from Eqs. 34 to 39). The computer predictions of the current efficiency with different operating conditions are shown in Figure 6.

The effect of the initial concentration of Na_2SO_4 on the current efficiency of acid or base production was shown in Figure 6a, b. These simulated results indicated that the current efficiency increased with the increase in the initial concentration of sodium sulfate, possibly because of an apparent increase in the conductivity of the electrolyte solution due to the increase of Na_2SO_4 concentration according to Eq. 28, which promotes the electromigration of the ions.

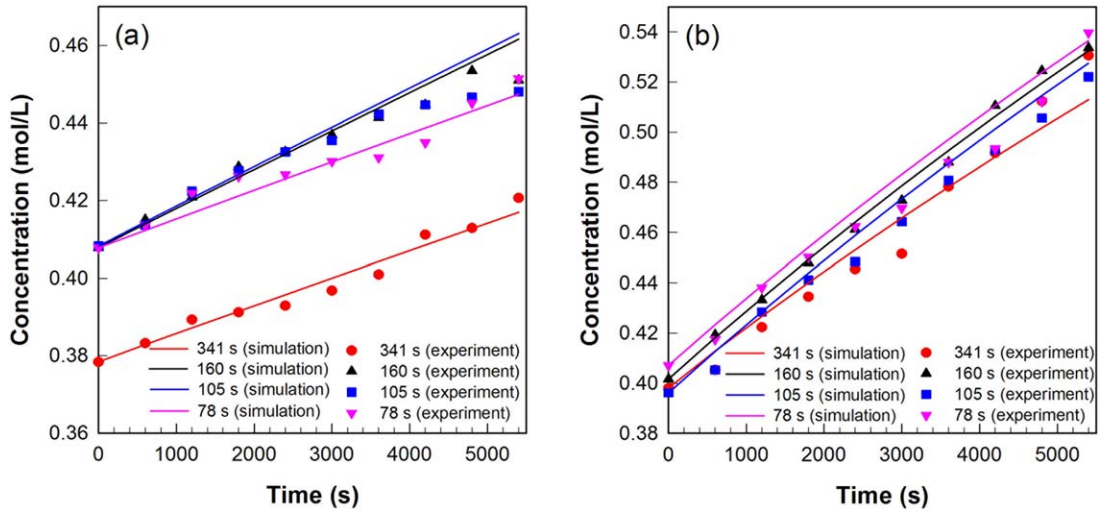

Figure 4. Acid and base outlet concentration profiles at different feed flow rates (5.70, 12.12, 18.48, and 24.84 L h^{-1}, equivalent to retention time of 341, 160, 105, and 78 s, respectively).

(a) Outlet concentration profiles of H_2SO_4 in the anode chamber compared with the experimental data and (b) Outlet concentration profiles of NaOH in the cathode chamber compared with the experimental data. [Color figure can be viewed in the online issue, which is available at wileyonlinelibrary.com.]

Additionally, an increase in the concentration gradient across the ion-exchange membrane is advantageous to the diffusion. This result can also be obtained from mathematic model inference. As mentioned in Eq. 33, the ion flux through the ion-exchange membrane was the sum of the migration and diffusion. The concentration difference ΔC in Eq. 33 was equivalent to $C_{1,\mathrm{mid}} - C_{1,\mathrm{cat}} - 2i(t_{1,\mathrm{m}} - t_1)\delta/D_1F$. Thus, a high value of $C_{1,\mathrm{mid}}$ will result in an increase in ΔC and enhance the diffusion. But, after a long-time running, the current efficiency of regeneration will be apparently decreased with the passage of time. One possible reason is that there exists a limiting value of regenerated product's concentration, which has been validated by the results in Figure 3, and some literatures also reported the similar phenomenon.[38,39] Therefore, with the increase of the concentration of NaOH in the cathode chamber, the sodium ions will probably diffuse reversely into the middle chamber due to the enlarging concentration gradient on both sides of the ion-exchange membrane. Conversely, the average current efficiency of regeneration agreed with the simulated results as shown in Figure 6g.

The effect of feed fluid flow rate on the current efficiency of acid and base generation was shown in Figure 6c, d, respectively. The results indicated that both the current efficiency of sulfuric acid and sodium hydroxide generation were higher at a feed flow rate of 12.12 L h^{-1} (retention time 160 s) and 18.48 L h^{-1} (retention time 105 s) than those at a feed flow rate of 5.70 L h^{-1} (341 s). This phenomenon could be explained as follows. The microbubbles formed by the oxygen and HERs at the interface of electrodes accumulated and formed larger bubbles in the electrolyte bulk for low feed flow rate, increasing the electrolyte's resistance due to the larger value of the void fraction ε in

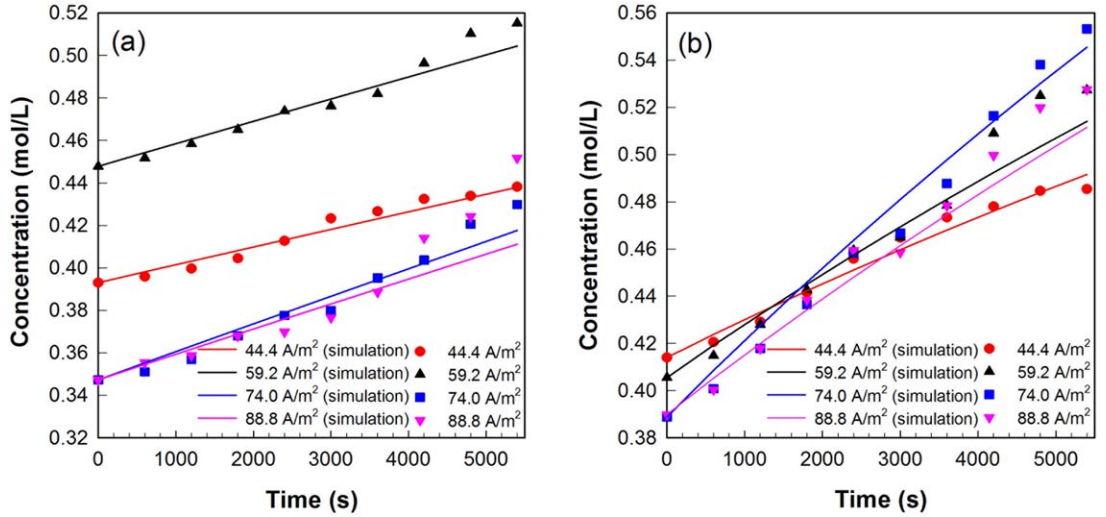

Figure 5. Acid and base outlet concentration profiles at different current densities.

(a) Outlet concentration profiles of H_2SO_4 in the anode chamber compared with the experimental data and (b) Outlet concentration profiles of NaOH in the cathode chamber compared with the experimental data. [Color figure can be viewed in the online issue, which is available at wileyonlinelibrary.com.]

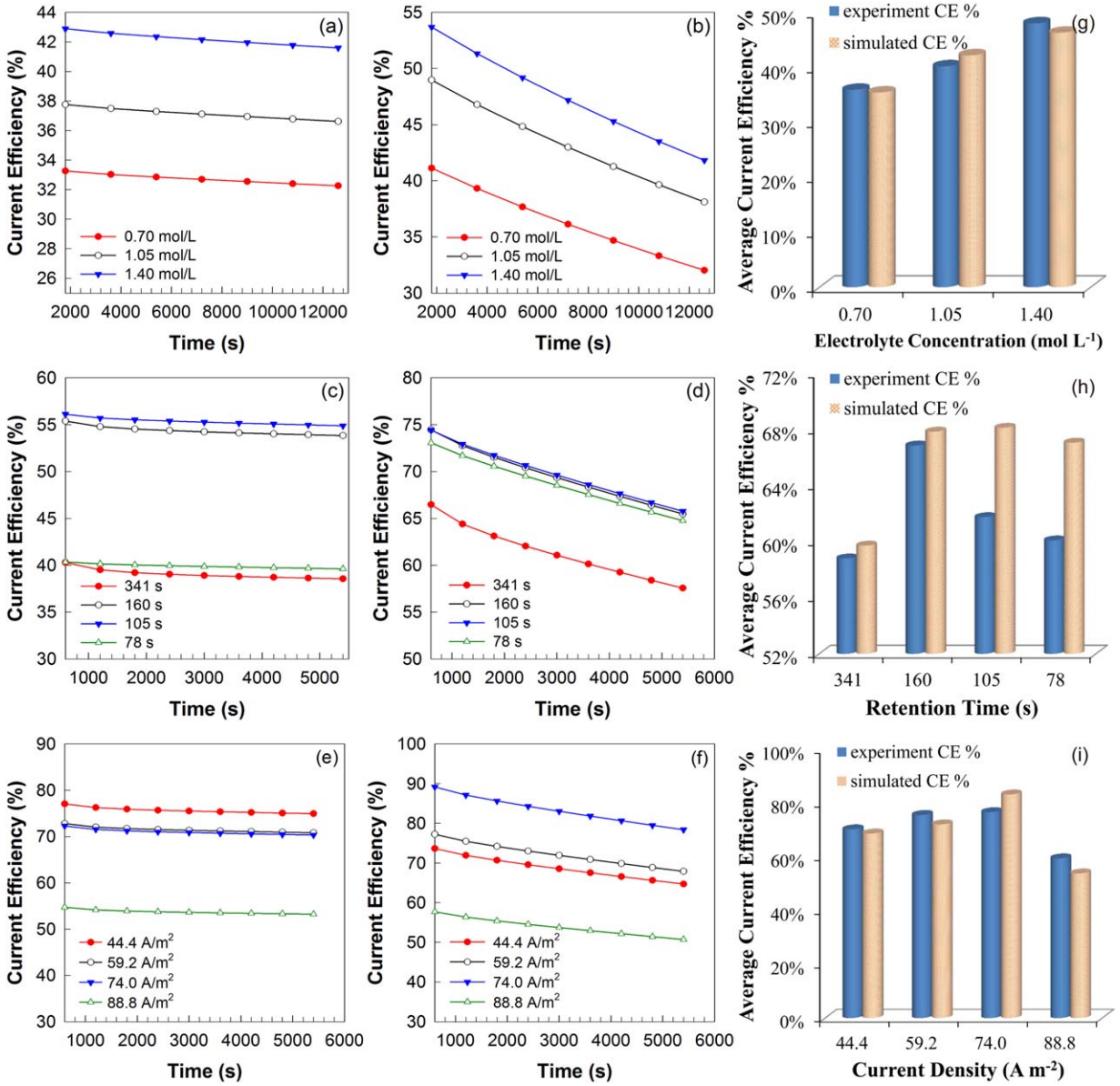

Figure 6. Computer predictions of the current efficiency with different operating conditions.

(a) and (b): the current efficiency for acid and base with different initial Na_2SO_4 concentrations, the initial acid and base concentrations were both 5% (by mass), the feed flow rate was 12.12 L h^{-1} (retention time 160 s) in all three compartments, and the current was 2.5 A. (c) and (d): the current efficiency for acid and base with different feed flow rates, $C_{o,H2SO4}$ = 0.4 mol L^{-1}, $C_{o,NaOH}$ = 0.4 mol L^{-1}, $C_{o,Na2SO4}$ = 1.0 mol L^{-1}, t = 25°C, and the current was 2.5 A. (e) and (f): the current efficiency of acid and base with different current density, $C_{o,H2SO4}$ = 0.4 mol L^{-1}, $C_{o,NaOH}$ = 0.4 mol L^{-1}, $C_{o,Na2SO4}$ = 1.0 mol L^{-1}, t = 25°C, and feed flow rate was 24.84 L h^{-1} (retention time 78 s). (g)–(i): comparisons of average current efficiencies between experiments and simulated results. [Color figure can be viewed in the online issue, which is available at wileyonlinelibrary.com.]

Eq. 27 and decreasing the effective reaction area of the electrodes.[40] On the contrary, the microbubbles could be quickly removed when the stirring rate was high. Generally, the mass transport number increases with the decrease in the thickness of the boundary layer due to the increasing stirring rate. However, as the stirring rate increases, the thickness of the boundary layer reaches a critical value. In this case, the mass transport number will not be changed significantly.[41]

Table 4. Performance Comparison Between the Designed Reactor in This Study and Mainstream Technologies of Chlor-Alkali Industry

	Current density (A m^{-2})	Cell voltage (V)	Current efficiency (%)	Predominant market
In this study (simulation, 25°C)	74.0	3.5–3.9	80–90 % (NaOH)	–
In this study (experiment, 25°C)	74.0	3.5–3.9	84% (NaOH)	–
Mercury cell process[44]	10^4	≈ 4.0	70–98% (depending on	Western Europe
Diaphragm cell process[44]	2–3 × 10^3	3.0–3.6	the technology used)	USA
Membrane cell process[44]	5 × 10^3	≈ 3.0		Japan
F. Farzami et al.[45]	2 × 10^3		76 % (25°C)−88 % (75°C)	Lab-scale

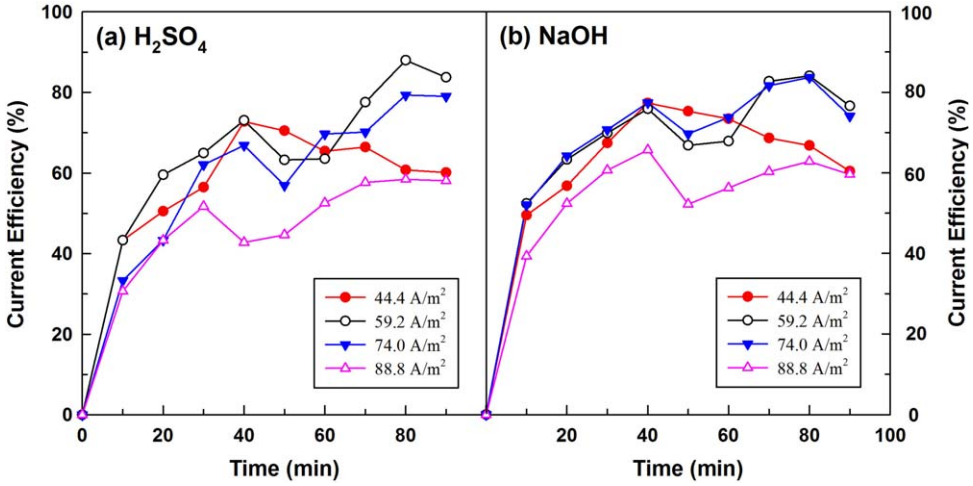

Figure 7. Current efficiency as a function of current density.

The other conditions were as follows: $C_{o,H2SO4}$ = 0.4 mol L^{-1}, $C_{o,NaOH}$ = 0.4 mol L^{-1}, $C_{o,Na2SO4}$ = 1.0 mol L^{-1}, t = 25°C, and the feed flow rate was 24.84 L h^{-1} (retention time 78 s). [Color figure can be viewed in the online issue, which is available at wileyonlinelibrary.com.]

When a feed flow rate is above the critical value, the bulk solution will be highly turbulent, which results in an apparent barrier of mass transfer along the x-axis at the interface of the electrodes and membranes. Practically, in Figure 6h, the experimental results also showed the similar trends with the results of simulation for alkali-sorbent regeneration. Therefore, it is not advantageous to apply a low feed fluid flow rate, and an overly high feed fluid flow rate hinders H_2SO_4 production, as shown in Figure 6c, while the decay of the current efficiency was not large for NaOH regeneration at high feed fluid flow rates both in experiments and numerical simulations, as shown in Figure 6d, h.

Furthermore, in Figure 6e, f, applying an appropriate current density produces a higher current efficiency, and all average current efficiencies under different current densities in the experiments agreed well with the numerical simulation results, as shown in Figure 6i. It is worth noticing that excessively high current density has negative effects on the performance of the electromembrane reactor. Because the bubble formation rate is dependent on the applied current density,[42] then rapid bubble formation may increase the gas void fraction leading to the increase in the resistances of the bulk solution and result in the drop in efficiency. Another possible reason of the performance reduction is that an increasing part of the total electrical energy is consumed to overcome the electrical resistances with the increase of the current density as reported by literatures.[43,44]

From the results of the computer predictions and comparisons to the experimental data mentioned above, it was concluded that a high concentration of Na_2SO_4 and an appropriate feed flow rate and current density would lead to an optimal performance of the lab-scale electromembrane reactor. Even more appealing, the current efficiency of NaOH regeneration could be as high as 80–90% in the computer predictions at a certain feed flow rate (24.84 L h^{-1}), as shown in Figure 6f, which is close to or higher than the average current efficiency of industrial or some lab-scale chlor-alkali reactor reported in literatures, as shown in Table 4. To verify this conclusion and the applicability of the optimization computations, experiments using the same conditions as in the computer prediction (conditions of Figure 6e, f) were performed. The experimental results, shown in Figure 7, indicated that the current efficiency of NaOH regeneration could be as high as approximately 84% and that the current efficiency of H_2SO_4 could reach 87%. This finding strongly indicates that the model proposed in this article for optimization is applicable and the method has the potential for further scale-up and application.

Estimate of energy consumption and production cost

The analysis of each produced commodity product associated with the energy consumption was provided in Table 5. The results indicated that the electricity requirement per tons of NaOH and H_2SO_4 was 3159.76 and 2657.31 kWh,

Table 5. Energy Consumption and Economic Analysis of the Designed Process

Results	Regeneration of NaOH	Sulfuric acid production	Hydrogen production	Oxygen production
Current efficiency	84.08%	79.35%	74.22 %	72.04 %
Energy consumption	3159.76 kWh/t	2657.31 kWh/t	10.33 kWh/m^{-3}	21.29 kWh/m^{-3}
Price of off-peak electricity ($/kWh)	0.04	0.04	0.04	0.04
Total cost for production[a]	777.64 RMB/T NaOH (126.39 $/t NaOH)	653.97 RMB/T H_2SO_4 (106.29 $/t H_2SO_4)	0.41 $/m^{-3} H_2 (5.06 $/kg H_2)	0.85 $/m^{-3} O_2 (0.65 $/kg O_2)

Operating parameters: i = 74.0 A m^{-2}, Cell voltage = 3.5 V, $C_{0,H2SO4}$ = 0.4 mol L^{-1}, $C_{0,NaOH}$ = 0.4 mol L^{-1}, $C_{0,Na2SO4}$ = 1.0 mol L^{-1}, feed flow rate was 24.84 L h^{-1} (retention time: 78 s) and t = 25°C.
The central parity of the exchange between RMB and USA dollars is 615.27 for every 100 USA dollars from the State Administration of Foreign Exchange, People's Republic of China, March 14, 2014.
The energy consumption E (kWh kg^{-1}) can be obtained as follows: $E = \int \frac{UIdt}{C_i VM}$

[a]$0.04/kWh represents very-low-cost/off-peak electricity price for economic analyses.

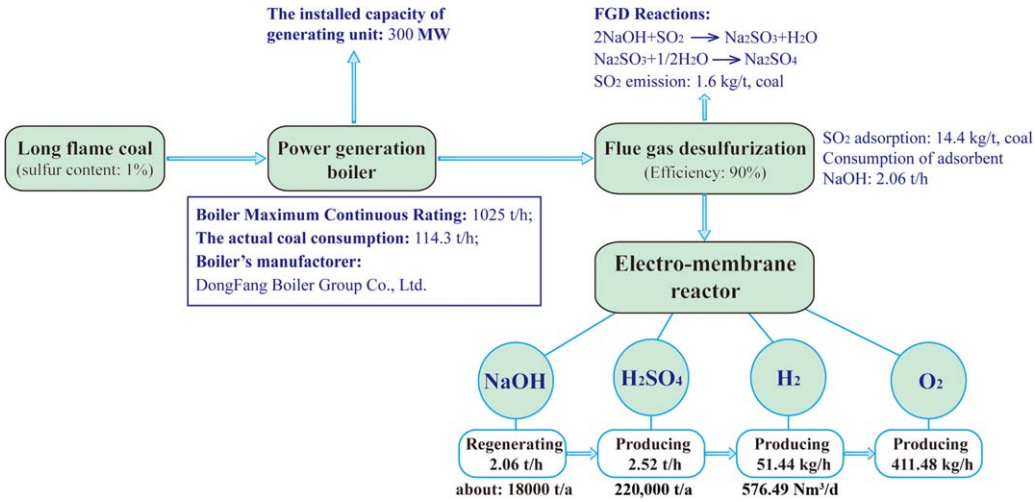

Scheme 1. A case calculation of a 300 MWh power generating unit.

[Color figure can be viewed in the online issue, which is available at wileyonlinelibrary.com.]

respectively, and the cost of NaOH regeneration was approximately 777.64 RMB/t NaOH (126.39 $/t NaOH), which is significantly lower than the average market price (3250–3300 RMB/t of 99% NaOH) in East China in September 2013. What is more appealing is that the cost of hydrogen production in this electromembrane reactor is $5.06/kg H_2 by using low-cost valley electricity, which is lower than the hydrogen selling price of $19.01/kg H_2[46] and slightly below the average industrial production cost of hydrogen ($6.92/kg H_2[47]). Conversely, the current efficiency of each product were all above 70% and as high as about 84% for NaOH regenerating process under the selected operating parameters.

Case calculation

A case calculation of a power generating unit with the capacity of 300 MW was illustrated in Scheme 1. The power generation boiler, manufactured by DongFang Boiler Group Co., consumes coal of 114.3 t/h as designed. The amount of SO_2 emission can be estimated by Eq. 45, according to the Chinese National Standards (HJ/T 69–2001)

$$K_{SO_2}=0.2S_{ar}\cdot P\cdot(1-\eta)(\text{kg/t coal}) \quad (45)$$

where S_{ar} is the percentage of sulfur content in the coal; P, with the value of 80 when S_{ar} is equal to 1%, is the content of combustible components in total sulfur; and η is the efficiency of the FGD. As shown in Scheme 1, the results of case calculation indicated that regenerating 2.06 t NaOH per hour would produce 2.52 t sulfuric acid, 51.44 kg hydrogen, and 411.48 kg oxygen. Based on these calculation results, approximate 220,000 t H_2SO_4 could be theoretically produced per year while approximate 576.49 Nm^3 hydrogen could be produced per hour, which hints the possibility of profit.

Conclusions

In conclusion, an efficient method was proposed to electrochemically regenerate NaOH sorbent and realize resource recovery of sulfur and clean energy production from FGD residuals. The optimization computations were then validated by experiments, which indicated that the current efficiency of alkali-sorbent regeneration could reach approximately 84% and the sulfur recovery as H_2SO_4 could reach 87%. These results showed a comparable or higher current efficiency than that of industry chlor-alkali reactors (~80% on average). Additionally, the procedure was a green electrochemical process and a potential way to dispose of FGD residuals. The cost could be greatly reduced using the inherently free surplus electricity of the power plant or low-cost valley electricity. The regenerated alkali-sorbent could be recycled in FGD process to improve the efficiency of desulfurization and the produced sulfuric acid is also a valuable by-product. Meanwhile, the air productions (oxygen and hydrogen) could make the process profitable.

Acknowledgments

This research is based upon work supported by the National Natural Science Foundation of China (Project No. 21277045), Key Projects in the National Science & Technology Pillar Program during 12th Five-year Plan (No. 2011BAZ01960), the Shanghai Leading Academic Discipline Project (Project No: B506) and the Fundamental Research Funds for the Central Universities. Any opinions, findings, conclusions, or recommendations expressed in this publication are those of the authors and do not necessarily reflect the view of the supporting organizations.

Literature Cited

1. Srivastava RK, Jozewicz W, Singer C. SO_2 scrubbing technologies: a review. *Environ Prog*. 2001;20:219−228.
2. Srivastava RK, Jozewicz W. Flue gas desulfurization: the state of the art. *J Air Waste Manage Assoc*. 2001;51:1676−1688.
3. Pandey RA, Biswas R, Chakrabarti T, Devotta S. Flue gas desulfurization: physicochemical and biotechnological approaches. *Crit Rev Environ Sci Technol*. 2005;35:571−622.
4. Liu Y, Bisson TM, Yang H, Xu Z. Recent developments in novel sorbents for flue gas clean up. *Fuel Process Technol*. 2010;91:1175−1197.
5. Bouhadana Y, Avraham E, Soffer A, Aurbach D. Several basic and practical aspects related to electrochemical deionization of water. *AIChE J*. 2010;56:779–789.
6. Cao X, Huang X, Liang P, Xiao K, Zhou Y, Zhang X, Logan BE. A new method for water desalination using microbial desalination cells. *Environ Sci Technol*. 2009;43:7148−7152.
7. Alkire RC, Braatz RD. Electrochemical engineering in an age of discovery and innovation. *AIChE J*. 2004;50:2000–2007.
8. Koter S, Warszawski A. Electromembrane processes in environment protection. *Pol J Environ Stud*. 2000;9:45–56.

9. Yang C, Hu Y, Cao L, Yang J. Circulating regeneration and resource recovery of flue gas desulfurization residuals using a membrane electroreactor: from lab concept to commercial scale. *Environ Sci Technol*. 2012;46:11273−11279.
10. Ibl N, Robertson PM. Optimisation of use of surplus night electricity in electrochemical processes. *Electrochim Acta*. 1973;18:897–906.
11. Rohman FS, Aziz N. Optimization of batch electrodialysis for hydrochloric acid recovery using orthogonal collocation method. *Desalination* 2011;275:37–49.
12. Morf WE, Pretsch E, de Rooij NF. Computer simulation of ion-selective membrane electrodes and related systems by finite-difference procedures. *J Electroanal Chem*. 2007;602:43−54.
13. Fidaleo M, Moresi M. Optimal strategy to model the electrodialytic recovery of a strong electrolyte. *J Membr Sci*. 2005;260:90−111.
14. Dydek EV, Bazant MZ. Nonlinear dynamics of ion concentration polarization in porous media: the leaky membrane model. *AIChE J*. 2013;59: 3539–3555.
15. Fidaleo M, Moresi M. Application of the Nernst-Planck approach to model the electrodialytic recovery of disodium itaconate. *J Membr Sci*. 2010;349:393−404.
16. Zeng K, Zhang DK. Recent progress in alkaline water electrolysis for hydrogen production and applications. *Prog Energy Combust Sci*. 2010;36:307–326.
17. Kim S, Koratkar N, Karabacak T, Lu TM. Water electrolysis activated by Ru nanorod array electrodes. *Appl Phys Lett*. 2006;88: 2631061−3.
18. Rossmeisl J, Logadottir A, Nørskov JK. Electrolysis of water on (oxidized) metal surfaces. *Chem Phys*. 2005;319:178–184.
19. Birry L, Lasia A. Studies of the hydrogen evolution reaction on raney nickel-molybdenum electrodes. *J Appl Electrochem*. 2004;34: 735–749.
20. Bocutti R, Saeki MJ, Florentino AO, Oliveira CLF, Ângelo ACD. The hydrogen evolution reaction on codeposited Ni–hydrogen storage intermetallic particles in alkaline medium. *Int J Hydrogen Energy*. 2000;25:1051–1058.
21. Sheng W, Gasteiger HA, Shao-Horn Y. Hydrogen oxidation and evolution reaction kinetics on platinum: acid vs alkaline electrolytes. *J Electrochem Soc*. 2010;157:B1529−B1536.
22. Elezović NR, Jović VD, Krstajić NV. Kinetics of the hydrogen evolution reaction on Fe-Mo film deposited on mild steel support in alkaline solution. *Electrochim Acta*. 2005;50:5594−5601.
23. De Faria LA, Boodts JFC, Trasatti S. Electrocatalytic properties of ternary oxide mixtures of composition $Ru_{0.3}Ti_{(0.7-x)}Ce_xO_2$: oxygen evolution from acidic solution. *J Appl Electrochem*. 1996;26: 1195−1199.
24. Hu JM, Zhang JQ, Cao CN. Oxygen evolution reaction on IrO2-based DSA® type electrodes: kinetics analysis of Tafel lines and EIS. *Int J Hydrogen Energy*. 2004;29:791–797.
25. Da Silva LM, Boodts JFC, De Faria LA. Oxygen evolution at RuO2(x)+Co3O4(1-x) electrodes from acid solution. *Electrochim Acta*. 2001;46:1369−1375.
26. Philippe M, Jérôme H, Sebastien B, Gérard P. Modelling and calculation of the current density distribution evolution at vertical gas-evolving electrodes. *Electrochim Acta*. 2005;51:1140−1156.
27. McCleskey RB. Electrical conductivity of electrolytes found in natural waters from (5 to 90) °C. *J Chem Eng Data*. 2011;56:317–327.
28. Mann RF, Amphlett JC, Hooper MAI, Jensen HM, Peppley BA, Roberge PR. Development and application of a generalised steady-state electrochemical model for a PEM fuel cell. *J Power Sources*. 2000;86:173−180.
29. Lee HJ, Sarfert F, Strathmann H, Moon SH. Designing of an electrodialysis desalination plant. *Desalination* 2002;142:267−286.
30. Bard AJ, Faulkner LR. Electrochemical methods: fundamentals and applications. In: Harris D, Swain E, Aiello E, eds. Mass Transfer by Migration and Diffusion, 2nd ed. NewYork: Wiley, 2001:138−140.
31. Larchet C, Nour S, Auclair B, Dammak L, Nikonenko V. Application of chronopotentiometry to determine the thickness of diffusion layer adjacent to an ion-exchange membrane under natural convection. *Adv Colloid Interface Sci*. 2008;139:45−61.
32. Ray P, Shahi VK, Pathak TV, Ramachandraiah G. Transport phenomenon as a function of counter and co-ions in solution: chronopotentiometric behavior of anion exchange membrane in different aqueous electrolyte solutions. *J Membr Sci*. 1999;160:243−254.
33. Huguet P, Kiva T, Noguera O, Sistat P, Nikonenko V. The crossed interdiffusion of sodium nitrate and sulfate through an anion exchange membrane, as studied by Raman spectroscopy. *New J Chem*. 2005;29:955−961.
34. Pérez-Herranz V, Guiñón JL, García-Antón J. A new technique for the visualization of the concentration boundary layer in an electrodialysis cell. *J Appl Electrochem*. 2000;30:809−816.
35. Conway BE, Jerkiewicz G. Relation of energies and coverages of underpotential and overpotential deposited H at Pt and other metals to the 'volcano curve' for cathodic H2 evolution kinetics. *Electrochim Acta*. 2000;45:4075−4083.
36. Kellenberger A, Vaszilcsin N, Brandl W, Duteanu N. Kinetics of hydrogen evolution reaction on skeleton nickel and nickel–titanium electrodes obtained by thermal arc spraying technique. *Int J Hydrogen Energy*. 2007;32:3258−3265.
37. Correa-Lozano B, Comninellis C, De Battisti A. Electrochemical properties of Ti/SnO2-Sb2O5 electrodes prepared by the spray pyrolysis technique. *J Appl Electrochem*. 1996;26:683−688.
38. Wang X, Wang Y, Zhang X, Xu T. In situ combination of fermentation and electrodialysis with bipolar membranes for the production of lactic acid: operational compatibility and uniformity. *Bioresour Technol*. 2012;125:165–171.
39. Kumar M, Tripathi BP, Saxena A, Shahi VK. Electrochemical membrane reactor: synthesis of quaternary ammonium hydroxide from its halide by in situ ion substitution. *Electrochim Acta*. 2009;54:1630–1637.
40. Mandin P, Wüthrich R, Roustan H. Polarization curves for an alkaline water electrolysis at a small pin vertical electrode to produce hydrogen. *AIChE J*. 2010;56:2446–2454.
41. Barrágan VM, Ruíz-Bauzá C. Current-voltage curves for ion-exchange membranes: a method for determining the limiting current density. *J Colloid Interface Sci*. 1998;205:365−373.
42. Wauters CN, Winnick J. Electrolytic membrane recovery of bromine from waste hydrogen bromide streams. *AIChE J*. 1998;44:2144–2148.
43. Huang C, Xu T, Jacobs ML. Regenerating flue-gas desulfurizing agents by bipolar membrane electrodialysis. *AIChE J*. 2006;52:393–401.
44. O'Brien TF, Bommaraju TV, Hine F. Handbook of Chlor-Alkali Technology. New York: Springer, 2005.
45. Joudaki E, Farzami F, Mahdavi V, Hashemi SJ. Performance evaluation of oxygen-depolarized cathode with PtPd/C electrocatalyst layer in advanced chlor-alkali cell. *Chem Eng Technol*. 2010;33:1525–1530.
46. Ivy J. Summary of Electrolytic Hydrogen Production [NREL of the U.S. Department Energy website] September 1, 2004. Available at: http://www.nrel.gov/docs/fy04osti/36734.pdf. Accessed on November 25, 2013.
47. Businelli N, Liang Y, Lu J, Mbise T, Shaw L, Song K, Soussan R, Tait A, Yang J, Zhou H, Zhu M. A Portable Hydrogen Generator for the Homemaker [Princeton University website] March 31, 2010. Available at: https://www.princeton.edu/∼iahe/Document/IAHE_H2Competition_Poster.pdf. Accessed on March 17, 2014.

Manuscript received Dec. 19, 2013, and revision received Mar. 20, 2014.